CHAPTER 4.6

Partition Curves

Brian Flintoff

The partition curve (also known as a Tromp curve, selectivity curve, efficiency curve, classification curve, or performance curve) is a standard and very useful way to empirically model physical separation systems. This includes separations based on particle size (screens, hydrocyclones, spiral or screw and rake classifiers, air classifiers, deslimers, etc.), particle density (dense medium vessels or cyclones, etc.), particle magnetic properties (magnetic separators), and particle electrostatic properties (electrostatic separators). The partition curve provides an empirically derived description of the separation process within a given system with respect to a specific feed property, such as particle size.

The emergence of multiphysics modeling and simulation tools (e.g., two-way coupled discrete element method and computational fluid dynamics) are leading to more fundamental descriptions based on first principles of the phenomena underpinning the partition curve in these various separators. Nevertheless, the empirical approach will remain as a core tool (1) in process analysis for plant engineers, (2) as an important decision-support tool in process design, and (3) as a key element of most process simulation software.

This chapter provides a relatively in-depth review of the partition curve including details on the data analysis steps. Since the hydrocyclone has a very rich history of study, and because it can exhibit some "unusual" analytical challenges, it will be used as the basis for the descriptive material that follows.

DATA ACQUISITION, SCREENING, AND MASS BALANCES

The construction of a partition curve from plant data requires that a sampling campaign (also known as a survey) be completed. The details around the design of experiments, the identification of good sampling points, the design of proper sample cutters, and the estimation of required sample weights, number of cuts and timing, and so on, are beyond the scope of this discussion. (For more information on these topics, the reader is referred to sources such as Wills and Finch 2016, or, where available, *The SPOC Manual* by Canada Centre for Mineral and Energy Technology [Laguitton 1985]). Suffice to say that, following these principles, two steady-state sampling campaigns were completed, as illustrated in Figure 1.

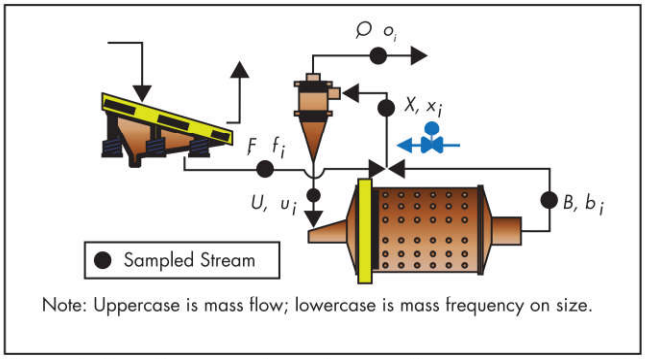

Figure 1 Sampling experiment in a semiautogenous and ball mill circuit

The grinding circuit in Figure 1 treats a low-grade copper ore with minimal gangue sulfides; that is, it is a relatively homogeneous rock displaying the physical properties of the predominant siliceous gangue. The two campaigns corresponded to plant operation treating both a soft (supergene) ore and a hard (hypogene) ore, and these designations are retained through this chapter. The raw data are presented in Tables 1 and 2.

Notice that a characteristic (geomean, or geometric mean) size has been assigned to the pan fraction, as indicated in boldface in these tables. This is derived by simply assigning a size of $s_{n-1}/3$ to the pan fraction, where s_{n-1} is the finest sieve aperture (often 400 mesh or 37 µm). This approximation, which is explained later, generally gives acceptable results when the partition curve is very well defined by the data, and it expedites the data processing step. However, there is an alternative approach for the pan fraction, which is discussed in the "Challenges with Very Fine Separations" section later in this chapter. In addition, to calculate the geomean size for the coarsest size class, it has been assumed that the upper limiting size (s_0) is 12,500 µm. Since in well-designed experiments the partition factor is always 1.0 in this size range, this assumption or calculation is not very important.

Brian Flintoff, Consultant, Sigmation Inc., Kelowna, British Columbia, Canada

Table 1 Soft ore sampling data

Stream		Screen Undersize (U)	Ball Mill Discharge (B)	Cyclone Feed (X)	Cyclone Overflow (O)	Cyclone Underflow (U)
Mass Flow, t/h		1,298.00				
% Solids		75.0	73.6	61.1	41.3	74.4
Passing Size, μm	Geomean Size, μm	Frequency, % retained	Frequency, % retained	Frequency, % retained	Frequency, % retained	Frequency, % retained
9,525	10,911.6	0.95	2.12	1.71	0.00	6.84
6,700	7,988.6	3.37	2.67	4.56	0.00	5.32
4,750	5,641.4	3.03	2.82	4.96	0.00	4.32
3,350	3,989.0	4.30	3.09	4.95	0.00	4.19
2,360	2,811.8	4.16	3.15	4.53	0.03	4.40
1,700	2,003.0	3.55	2.27	2.59	0.12	3.41
1,180	1,416.3	4.95	3.75	4.20	0.18	5.38
850	1,001.5	4.23	3.96	4.16	0.15	5.52
600	714.1	5.24	6.77	6.58	0.24	8.45
425	505.0	5.65	10.48	9.36	0.70	11.88
300	357.1	5.96	11.81	10.46	4.12	12.06
212	252.2	7.23	9.28	8.83	9.10	8.67
150	178.3	6.24	7.16	6.85	10.45	4.43
105	125.5	6.64	5.91	5.33	10.85	3.73
74	88.1	3.97	3.26	2.62	8.68	1.83
53	62.6	4.00	2.59	2.19	7.12	1.70
38	44.9	2.54	1.91	1.47	5.77	0.92
Pan	**12.3**	23.99	17.00	14.65	42.49	6.95
Checks		100.00	100.00	100.00	100.00	100.00

Table 2 Hard ore sampling data

Stream		Screen Undersize (U)	Ball Mill Discharge (B)	Cyclone Feed (X)	Cyclone Overflow (O)	Cyclone Underflow (U)
Mass Flow, t/h		738.00				
% Solids		59.5	67.0	52.1	29.6	72.1
Passing Size, μm	Geomean Size, μm	Frequency, % retained	Frequency, % retained	Frequency, % retained	Frequency, % retained	Frequency, % retained
9,525	10,911.6	5.20	0.79	1.97	0.00	1.67
6,700	7,988.6	5.91	1.08	2.28	0.00	3.72
4,750	5,641.4	5.78	1.64	2.47	0.00	2.97
3,350	3,989.0	6.74	1.48	2.73	0.00	3.16
2,360	2,811.8	6.80	1.67	2.61	0.00	3.11
1,700	2,003.0	3.11	1.63	2.76	0.00	3.15
1,180	1,416.3	5.18	2.43	3.46	0.00	4.56
850	1,001.5	4.10	2.51	3.14	0.00	4.06
600	714.1	4.88	3.98	4.26	0.19	5.98
425	505.0	5.22	6.39	5.88	0.14	8.52
300	357.1	5.08	10.33	8.58	0.46	12.29
212	252.2	5.13	17.57	13.75	3.24	15.99
150	178.3	5.25	10.81	9.16	11.96	10.61
105	125.5	4.86	9.32	7.97	13.78	6.22
74	88.1	2.72	4.92	4.43	8.68	3.31
53	62.6	2.31	4.43	4.08	7.17	1.86
38	44.9	1.79	2.40	2.31	5.40	1.09
Pan	**12.3**	19.94	16.62	18.16	48.98	7.73
Checks		100.00	100.00	100.00	100.00	100.00

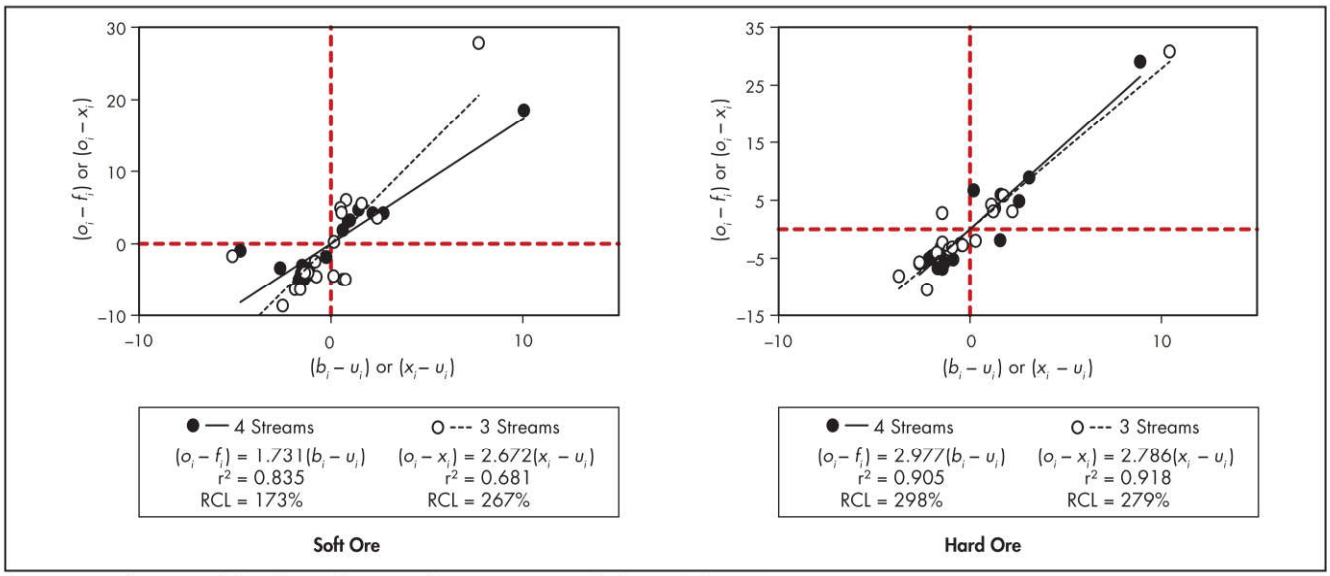

Figure 2 Soft ore and hard ore data—rudimentary mass balance information

Parameter estimation from mass balanced (or massaged) data tends to give better estimates (i.e., minimum variance) than simply using the raw data (Wiegel 1979; Hodouin et al. 1984). Consequently, many operations routinely use the material balance software available in simulation packages (e.g., JKSimMet or USIM PAC) or stand-alone balancing packages (e.g., Algosys Bilmat or Metso MetTools) to process the sample data. In the absence of this kind of software, another less rigorous (and less accurate) method can be used. The authors frequently recommend that this step be conducted in any event, as it gives a good indication of the quality of the data—the so-called data screening step. No mass balance package can "clean" a highly corrupt sample data set—the garbage in, garbage out principle. In such cases, it is usually best to redo the experiment rather than waste a lot of time in data processing and ultimately produce questionable results.

Using the symbology of Figure 1, the basic equation for the experimental partition factor is given in Equation 1. A plot of p_i versus the characteristic size yields the partition curve:

$$p_i = \frac{Uu_i}{Xx_i} = \left[\frac{U}{X}\right]\left[\frac{u_i}{x_i}\right] \quad \textbf{(EQ 1)}$$

where

p_i = partition factor for size class i (the fraction of the feed material in this size class that reports to the underflow or coarse stream)
U = mass flow of solids to the underflow or coarse stream
u_i = mass frequency in size class i in the underflow or coarse stream
X = mass flow of solids in the hydrocyclone feed stream
x_i = mass frequency in size class i in the feed stream

For data screening or to estimate a more rudimentary mass balance (e.g., to deduce the mass split, U/X, in Equation 1), the approach is to develop the basic steady-state mass balance equations for the flow sheet in Figure 1. Since we cannot accommodate "redundant" data, two options are available that relate to the hydrocyclone partition curve. One involves three streams (X, U, and O) and the other involves four streams (F, B, U, and O), and these are treated separately in the following equations.

Three-stream balance:

$$X = U + O \quad \textbf{(EQ 2)}$$

$$Xx_i = Uu_i + Oo_i \quad \textbf{(EQ 3)}$$

therefore,

$$(o_i - x_i) = \frac{U}{O}(x_i - u_i) \quad \textbf{(EQ 4)}$$

Four-stream balance:

$$F + B = U + O \text{ and } F = O \text{ and } B = U \quad \textbf{(EQ 5)}$$

$$Ff_i + Bb_i = Uu_i + Oo_i \quad \textbf{(EQ 6)}$$

therefore,

$$(o_i - f_i) = \frac{U}{O}(b_i - u_i) \quad \textbf{(EQ 7)}$$

where

O = mass flow of solids in the overflow or fine stream
o_i = mass frequency in size class i in the overflow or fine stream
F = mass flow of solids in the screen undersize or fresh feed stream
f_i = mass frequency in size class i in the fresh feed stream
B = mass flow of solids in the ball mill discharge stream
b_i = mass frequency in size class i in the ball mill discharge stream

Plots of Equations 4 and 7 will give a good visualization of the data quality as well as an estimate of the recirculating load (RCL = U/O). Figure 2 shows the results for the data in Tables 1 and 2, and the RCL is reported as both fractional and

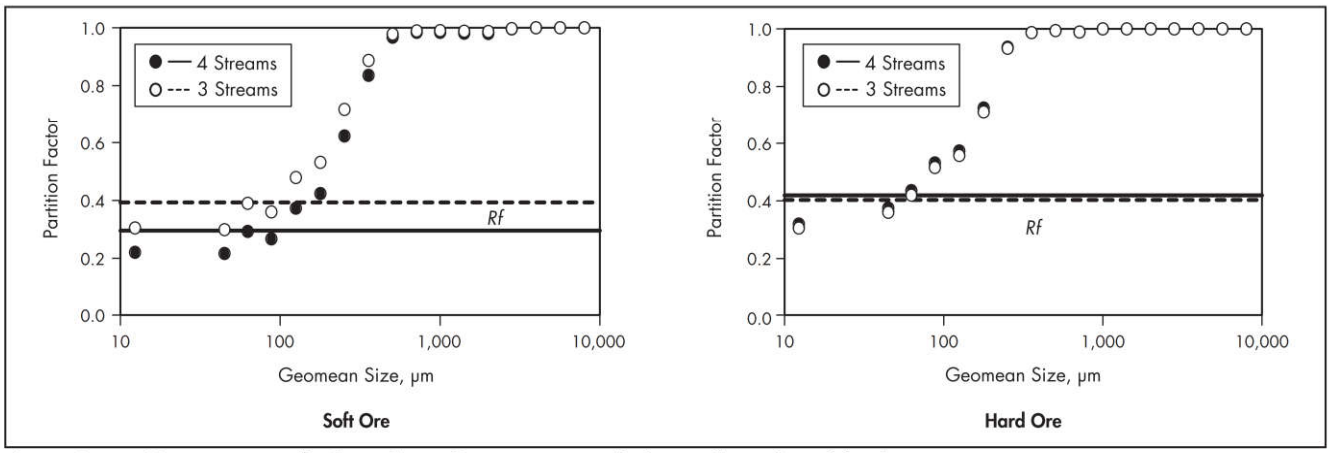

Figure 3 Partition curve results from the rudimentary mass balances for soft and hard ores

percentage values. (Note that for these kinds of plots involving the differences in mass frequency vectors [e.g., $x_i - u_i$], by definition, they must pass through the point [0,0]; hence, the use of a regression that forces the constant to zero.)

It is quite clear from Figure 2 that the hard ore data are of higher quality (better r^2, greater consistency in the recirculating load estimates, visually less data scatter, better agreement of the two methods, etc.). From a data screening point of view, a mass balance will be more difficult on the soft ore and some additional analysis would be required to try to deduce which stream(s) is likely the problem. This stream(s) would then be given less weight in the mass balance solution.

To complete this discussion, the partition factors can be calculated using the (fractional) estimates of the recirculating load value according to Equation 8 and are shown in Figure 3. It is generally good practice to use the underflow and overflow streams for these calculations, as they afford a better definition of the partition curve in the coarse and fine size ranges.

$$p_i = \frac{(\mathrm{RCL})(u_i)}{(\mathrm{RCL})(u_i)+(1)(o_i)} \qquad \textbf{(EQ 8)}$$

The parameter *Rf*, shown as the horizontal lines in Figure 3, is discussed later in this chapter, but it is the mass recovery of water from the hydrocyclone feed stream to the underflow stream, or

$$Rf = \frac{(\mathrm{RCL})\left(100/u' - 1\right)}{(\mathrm{RCL})\left(100/u' - 1\right)+(1)\left(100/o' - 1\right)} \qquad \textbf{(EQ 9)}$$

where

u' = % solids in the underflow stream
o' = % solids in the overflow stream

For a homogeneous ore in a typical grinding circuit application, the partition factor in the very fine sizes should be quite comparable to *Rf* (i.e., the fine particles behave as part of the fluid). From Figure 3, it is again clear that the hard ore data conform better to this expectation than do the soft ore data.

A detailed discussion on the mechanics of mass balance solutions is beyond the scope of this chapter. (The interested reader could refer to some of the foundational works [e.g., Mular 1979 or Hodouin et al. 1981].) Suffice to say that the adjusted data satisfy all of the mass balance equations (e.g., Equations 2, 3, 5, and 6) and in such a way that the adjustments on all measured data are minimized, in the weighted least-squares sense. Tables 3 and 4 present the mass balance results for the raw data in Tables 1 and 2, respectively. The partition curves for the mass balanced data are shown in Figure 4.

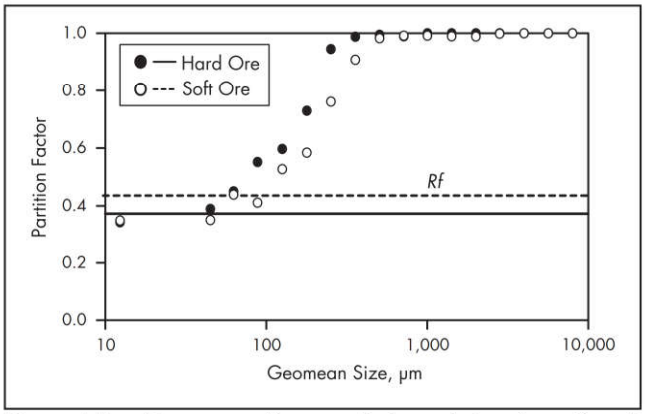

Figure 4 Partition curves for mass balanced data for soft and hard ores

To conclude this section, Figure 5 compares the partition curves from the rudimentary data to those from the mass balanced data. It is clear that for the soft ore (the more problematic data set), significant adjustments in the raw data were made, and even in this case there are still inconsistencies. However, for the hard ore (the better-quality data set), there is generally good agreement between the rudimentary and mass balanced data. This demonstrates the importance of good data screening, followed by mass balancing, to fully understand the quality of the resulting partition curve analysis.

Since the remaining analysis in this chapter utilizes the mass balanced data, henceforth the output from the mass balancing exercise is referred to as simply the *experimental data*.

PARTITION CURVE MODELING AND CURVE FITTING

The preceding partition curve data are interesting in the sense that one can qualitatively assess performance based on factors such as the amount of fine material bypassed to the underflow stream (*Rf*), the sharpness of the separation (e.g., the steepest

Table 3 Mass balance results for soft ore

Stream		Screen Undersize (U)	Ball Mill Discharge (B)	Cyclone Feed (X)	Cyclone Overflow (O)	Cyclone Underflow (U)
Mass Flow, t/h		1,298.00	4,022.39	5,320.39	1,298.00	4,022.39
% Solids		75.0	73.7	61.8	41.1	73.7
Passing Size, µm	Geomean Size, µm	Frequency, % retained	Frequency, % retained	Frequency, % retained	Frequency, % retained	Frequency, % retained
9,525	10,911.6	0.96	2.29	1.97	—	2.60
6,700	7,988.6	3.70	3.29	3.39	—	4.48
4,750	5,641.4	3.23	3.32	3.30	—	4.36
3,350	3,989.0	4.46	3.32	3.60	—	4.76
2,360	2,811.8	4.33	3.41	3.64	0.03	4.80
1,700	2,003.0	3.60	2.31	2.63	0.12	3.43
1,180	1,416.3	5.06	3.91	4.19	0.18	5.48
850	1,001.5	4.32	4.16	4.20	0.15	5.51
600	714.1	5.34	7.13	6.69	0.24	8.77
425	505.0	5.74	11.05	9.75	0.70	12.67
300	357.1	6.05	12.43	10.87	4.09	13.06
212	252.2	7.37	9.68	9.12	8.95	9.17
150	178.3	6.15	6.62	6.50	11.09	5.02
105	125.5	6.50	5.44	5.70	11.05	3.97
74	88.1	3.86	3.00	3.21	7.75	1.74
53	62.6	3.85	2.37	2.73	6.28	1.59
38	44.9	2.42	1.69	1.87	4.96	0.87
Pan	**12.3**	23.07	14.58	16.65	44.40	7.70
Checks		100.00	100.00	100.00	100.00	100.00

Table 4 Mass balance results for hard ore

Stream		Screen Undersize (U)	Ball Mill Discharge (B)	Cyclone Feed (X)	Cyclone Overflow (O)	Cyclone Underflow (U)
Mass Flow, t/h		738.00	2,355.85	3,093.85	738.00	2,355.85
% Solids		59.5	69.2	52.4	29.5	69.2
Passing Size, µm	Geomean Size, µm	Frequency, % retained	Frequency, % retained	Frequency, % retained	Frequency, % retained	Frequency, % retained
9,525	10,911.6	4.45	0.73	1.62	—	2.13
6,700	7,988.6	6.34	1.12	2.37	—	3.11
4,750	5,641.4	5.48	1.55	2.49	—	3.27
3,350	3,989.0	6.51	1.44	2.65	—	3.48
2,360	2,811.8	6.23	1.55	2.67	—	3.50
1,700	2,003.0	3.37	1.85	2.21	—	2.91
1,180	1,416.3	5.44	2.60	3.28	—	4.30
850	1,001.5	4.22	2.64	3.01	—	3.96
600	714.1	4.98	4.14	4.34	0.19	5.64
425	505.0	5.27	6.49	6.20	0.14	8.10
300	357.1	5.11	10.41	9.15	0.46	11.87
212	252.2	5.14	16.78	14.00	3.24	17.37
150	178.3	5.33	11.46	9.99	11.34	9.57
105	125.5	4.87	9.15	8.13	13.74	6.37
74	88.1	2.74	5.05	4.50	8.47	3.26
53	62.6	2.27	3.87	3.49	8.05	2.06
38	44.9	1.78	2.33	2.20	5.64	1.13
Pan	**12.3**	20.46	16.83	17.70	48.73	7.98
Checks		100.00	100.00	100.00	100.00	100.00

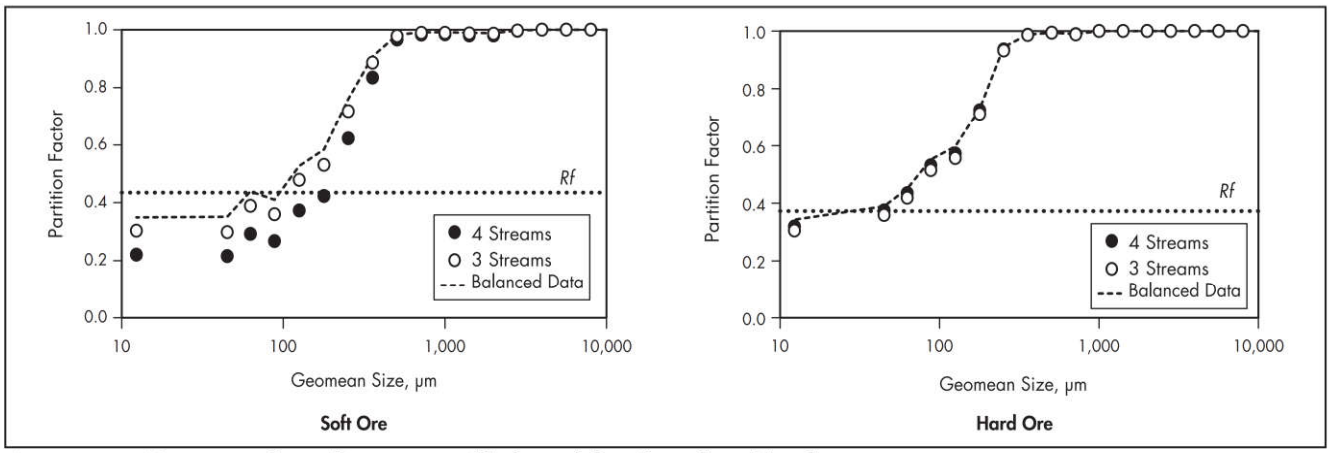

Figure 5 Partition curves for rudimentary and balanced data for soft and hard ores

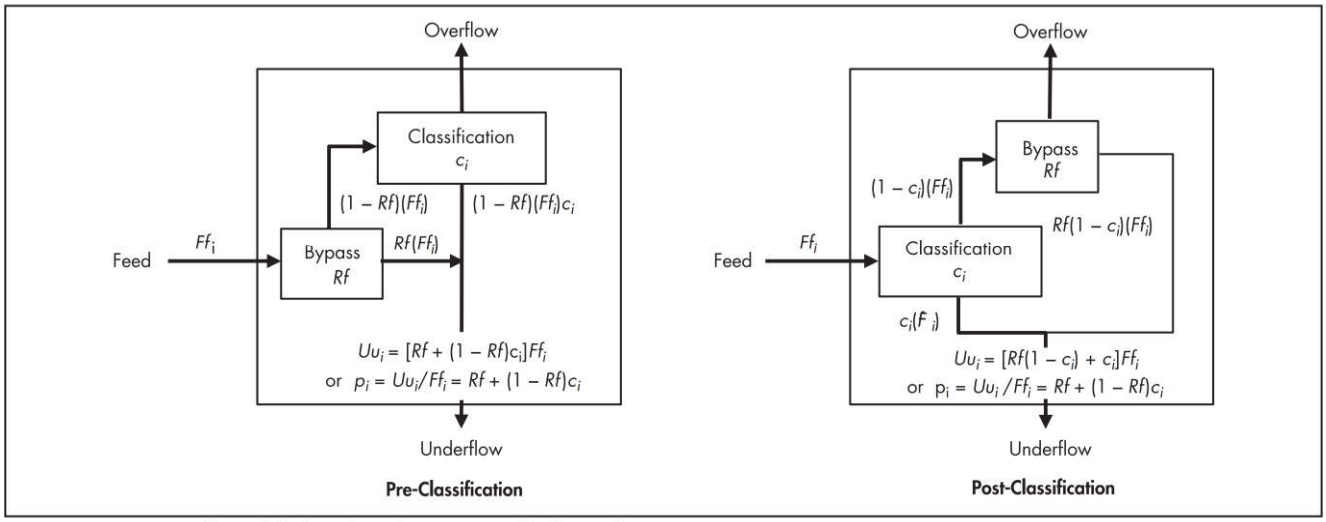

Figure 6 Conceptual models for classification in a hydrocyclone

slope of the partition curve), and effective separation or cut size (e.g., the size at which a particle has a 50% probability of reporting to the underflow stream). Quantitatively, mathematical models are a useful vehicle for data reduction, as the model parameters can provide direct measures of the performance metrics.

Usually there is some conceptual or phenomenological notion(s) that underpins the form of a mathematical model. In the case of the partition curve for a hydrocyclone, the two conceptual models that have been cited are illustrated in Figure 6. Here, a fraction (Rf) of the feed solids (pre-classification) or the overflow solids (post-classification) is bypassed to the underflow stream.

To briefly digress, the preceding conceptual models do not account for another mechanism that is sometimes seen in cyclone performance—the short-circuiting of coarse material across the upper regions of the inlet and into the overflow stream. This mechanism was more common with older cyclone inlet designs and in cases involving vortex finder wear/length issues. The experimental partition curve can give an indication that this may be a performance issue, for example, if the partition factors in the coarser size ranges do not approach the value of 1.0 as quickly as might be expected in this size range (e.g., an apparent offset). Normally this is not an important factor, at least from a partition modeling perspective. However, original equipment manufacturers have noted that new inlet designs effectively eliminate this problem.

Regardless of the way one chooses to think about it, the mass balance calculations in Figure 6 show that the general form of the hydrocyclone partition curve model is

$$\hat{p}_i = Rf + (1 - Rf)c_i \qquad \textbf{(EQ 10)}$$

where

$\hat{p}_i$ = predicted partition factor value from the model
Rf = mass fraction of water in the feed stream that reports to the underflow stream
c_i = "corrected" classification partition factor value (i.e., corrected for the bypass, Rf)

As the preceding partition curve figures show, the curve looks sigmoidal in nature, so it is no surprise that quite a number of functional forms have been used to describe c_i. A few of these are summarized in Equations 11 through 16, but the two most common forms are the Rosin–Rammler function used

by Plitt (Equation 11—see Plitt 1971; the equation below is shown in a slightly different form than that of Plitt) and the exponential sum function used by Lynch–Rao (Equation 12—see Lynch and Rao 1975). Equations 13 and 14 are variations on the logistic function, which has been used in electrostatic separation (Wei and Realff 2005), Equation 15 is the log normal function, and Equation 16 is an arctangent function that has been used for coal partition curves (De Lange and Venter 1987).

$$c_i = 1 - 0.5^{\left(d_i / d50c\right)^{\alpha}} \quad \textbf{(EQ 11)}$$

$$c_i = \frac{\exp\left(\alpha\left[d_i / d50c\right]\right) - 1}{\exp\left(\alpha\left[d_i / d50c\right]\right) + \exp\left(\alpha\right) - 2} \quad \textbf{(EQ 12)}$$

$$c_i = \frac{1}{1 + \left(d_i / d50c\right)^{-\alpha}} \quad \textbf{(EQ 13)}$$

$$c_i = \frac{1}{1 + \exp(-\alpha(d_i - d50c))} \quad \textbf{(EQ 14)}$$

$$c_i = 0.5 + 0.5\left[\mathrm{ERF}\left(\frac{(\ln(d_i) - \ln(d50c))}{\sqrt{2}\ \ln(\alpha)}\right)\right] \quad \text{for } d_i > d50c$$

$$c_i = 0.5 - 0.5\left[\mathrm{ERF}\left(\frac{(\ln(d50c) - \ln(d_i))}{\sqrt{2}\ \ln(\alpha)}\right)\right] \quad \text{for } d_i \le d50c \quad \textbf{(EQ 15)}$$

$$c_i = 0.5\left(\arctan\left[\alpha\left(d_i - d50c\right) + 1/\pi\right]\right) \quad \textbf{(EQ 16)}$$

where

d_i = characteristic size of size class i (defined in the following paragraph)
$d50c$ = corrected cut size parameter (i.e., the size at which $c_i = 0.5$)
α = sharpness-of-separation parameter in most of the preceding cases
ERF = Excel error function

Just as many models are used to describe c_i, there are different ways to define the average (e.g., mass mean) or characteristic size of a size class. The convention is to number the size classes from the coarsest ($i = 1$) to the finest ($i = n$), and Equations 17 through 19 define the three most common characteristic sizes: geomean, arithmetic mean, and bottom size (or top size), respectively. The most commonly encountered is the geomean size, which is what has been used in this chapter.

$$d_i = \sqrt{s_{i-1} s_i} \quad \textbf{(EQ 17)}$$

$$d_i = \frac{(s_{i-1} + s_i)}{2} \quad \textbf{(EQ 18)}$$

$$d_i = s_i \quad \textbf{(EQ 19)}$$

where

s_i = lower size limit for size class i (s_{i-1} is the upper limit)

Common practice is to employ a $\sqrt{2}$ series (i.e., $s_{i-1} = \sqrt{2}\, s_i$) for selecting the sieve sizes, as was the case for the preceding soft and hard ore data. An approximation, such as $d_{\text{pan}} \approx s_{n-1}/3$ is used for the pan fraction.

Table 5 Model fits for the hard ore data

Model for c_i	RSS	α	$d50c$	Rf
Equation 11	5.73E-03	1.84	144	0.35
Equation 12	5.50E-03	2.27	143	0.33
Equation 13	1.15E-02	2.78	142	0.37
Equation 14	5.50E-03	0.02	129	0.25
Equation 15	1.08E-02	1.85	141	0.37
Equation 16	1.62E-02	0.02	133	0.27

Fitting the model (Equation 10) to the raw or balanced data is a nonlinear least-squares problem—pick the parameters that minimize RSS below—that can be achieved using tools like Solver in Excel. The general weighted least-squares objective function is given by the following equation:

$$\mathrm{RSS} = \sum_{i=1}^{n} w_i \left[p_i - \hat{p}_i\right]^2 \quad \textbf{(EQ 20)}$$

where

RSS = residual sum of squares (unexplained variation in the experimental p_i data)
w_i = weighting factor for size class i (generally an unweighted RSS is used where all $w_i = 1$)

Equation 10 can represent a two-parameter (α, $d50c$) or three-parameter (α, $d50c$, Rf) estimation problem, although if the raw data are truly coherent, the two-parameter model is usually selected and Rf is computed from the mass balance results for water. (In this context, *coherent* means the degree to which the raw data satisfy the mass balance equations. For example, from Figure 2, the hard ore data are more coherent than the soft ore data. Mass balancing renders all the data coherent.) Nevertheless, it is often instructive to fit both forms of the model and then test to see if there is a statistically significant difference in the goodness of fit.

Table 5 presents the fits of the various three-parameter models to the hard ore data. All of the models do a reasonable job of describing the partition curve from the hard ore experimental data. However, only a couple of them provide reasonable agreement with the experimental Rf value and demonstrate the best fits. Specifically, these are the Plitt (Equation 11) or the Lynch–Rao (Equation 12) expressions for c_i, which are then used in Equation 10. For these two equations, the $d50c$ value is very similar, but the α values differ. This difference in the sharpness of separation is consistent for these two models (i.e., the Equation 12 α value is always slightly higher). That is to say, the α's cannot be compared between these two models, so once a functional form for c_i has been chosen, it is best to keep with it. In this chapter, the author uses Equation 11 for c_i, giving Equation 21 as the final partition curve model:

$$\hat{p}_i = Rf + (1 - Rf)\left[1 - 0.5^{\left(d_i / d50c\right)^{\alpha}}\right] \quad \textbf{(EQ 21)}$$

Figure 7 shows the fits of the model in Equation 21 to the experimental partition curve data from the mass balances in Tables 3 and 4. Generally, the goodness of fit is reasonable in both cases, but for the soft ore there is a significant discrepancy in the experimental Rf (from the water balance—0.435) and model Rf (from the size data—0.352) values. As a side note, in the case where the percentage of solids data is not available, or is not used in the mass balance (e.g., obviously

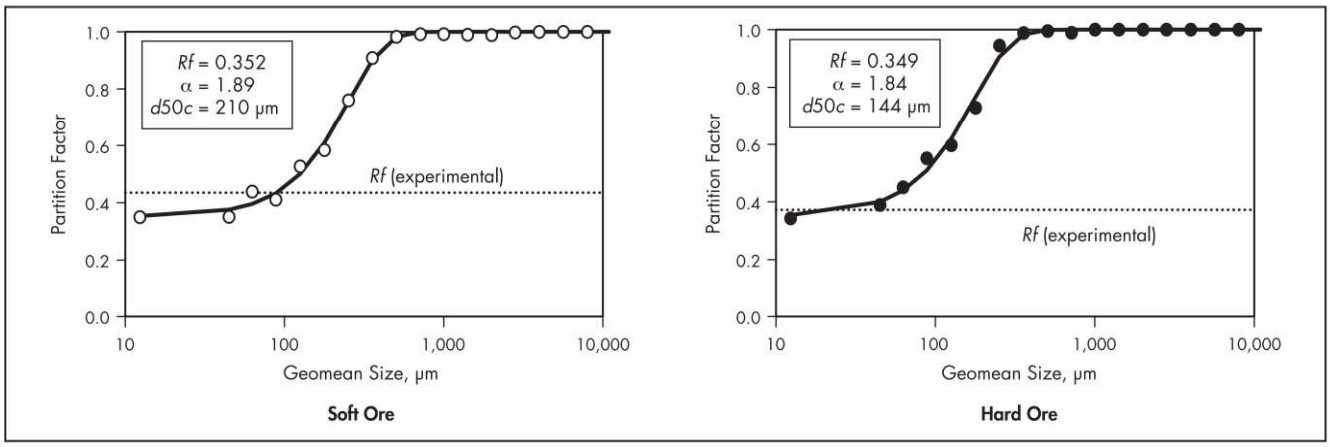

Figure 7 Partition curve model fits for soft and hard ores using experimental data

corrupt measurements), then *Rf* must be estimated from the particle size data.

Turning briefly to the statistical comparison of two- versus three-parameter models, one can apply the Partial F test. In general, the Partial F test compares calculated and tabulated F statistics to deduce whether estimating additional parameters in a model is statistically justified. Equations 22 and 23 show the two *F* statistics:

$$F_{\text{tabulated}} = F(0.05, k_2 - k_1, n - k_2) \quad \textbf{(EQ 22)}$$

$$F_{\text{calculated}} = \left[\frac{\dfrac{\text{RSS}(k_1) - \text{RSS}(k_2)}{(k_2 - k_1)}}{\dfrac{\text{RSS}(k_2)}{(n - k_2)}} \right] \quad \textbf{(EQ 23)}$$

where

k_1 = number of parameters in the most parsimonious model (here, $k_1 = 2$)
k_2 = number of parameters in the "new" model (here, $k_2 = 3$)
n = number of data points to be fit (here, $n = 18$)

In the case of the hard ore, the unweighted residual sum of squares values are RSS(2) = 6.34×10^{-3} and RSS(3) = 5.73×10^{-3}. Applying the preceding equations, $F_{\text{calculated}} = 1.58$ and $F_{\text{tabulated}} = 4.54$, and since the latter is greater than the former, there is no statistical justification for estimating *Rf* from the size data over simply using the experimental value for the hard ore data. That is the expected outcome when the raw data are coherent.

However, for the soft ore, the situation is reversed, with RSS(2) = 1.97×10^{-2} and RSS(3) = 4.79×10^{-3}, giving $F_{\text{calculated}} = 46.8$ and $F_{\text{tabulated}} = 4.54$. In this case, the estimation of the *Rf* parameter leads to a statistically superior fit. Such an outcome requires additional investigative work to determine if the data set can be used or whether the experiment must be repeated. As an example, it is sometimes the case that in sampling a hydrocyclone underflow stream, the cutter overfills and fine material is washed out—that is, the sample is biased coarse. This could be one reason that the partition curve model estimate of *Rf* is lower than the experimental value from the water balance. However, one might also expect the underflow sample % solids to also be biased high in this case, which would likely serve to reduce the experimental *Rf* value. It is a complex forensic problem, and anecdotal information from the persons cutting the samples *may* help rule such factors in or out. Clearly, if the preceding soft ore results are retained, they would have to be discounted relative to the hard ore results.

Table 6 Parameter standard error estimates

Parameter	Value	Standard Error	Coefficient of Variation, %
Rf	0.349	0.018	5.2
α	1.84	0.164	8.9
d50c	144	5.950	4.1
RSS	5.73E-03	—	—

Table 7 Parameter correlation

	Rf	α	*d50c*
Rf	1	0.71	0.77
α	0.71	1	0.61
d50c	0.77	0.61	1

Continuing with statistical considerations, the generalized nonlinear regression packages often provide estimates of parameter standard errors and of covariance/correlation matrices, which can be quite informative. Add-ins are available for Excel (e.g., de Levie 1999), which the chapter author would recommend to the reader. For illustrative purposes, Tables 6 and 7 present the standard errors for the three-parameter model and the parameter correlation matrix, respectively. The approximate 95% confidence limits on the parameters are approximately ±2 times the standard error. For example, the approximate 95% confidence limits on *d50c* are from 132 to 156 μm. The value of these standard errors is just to quantify the effects of data scatter on parameter precision. While it may be an arcane observation, these confidence limits need to be used with caution if one wishes to define, say, a parameter space (i.e., a "rectangular region" defining expected parameter values). As discussed briefly in the text that follows, the significant covariance of these parameters distorts the joint confidence limits.

As is usually the case with nonlinear models, there is a relatively high degree of correlation in the parameters, as

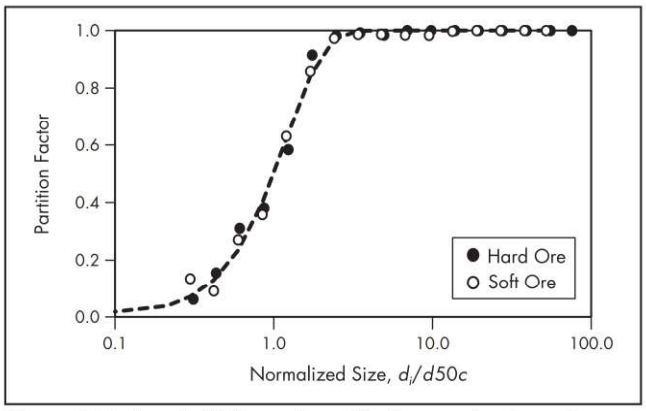

Figure 8 Reduced efficiency (partition) curve for the soft and hard ore balanced data

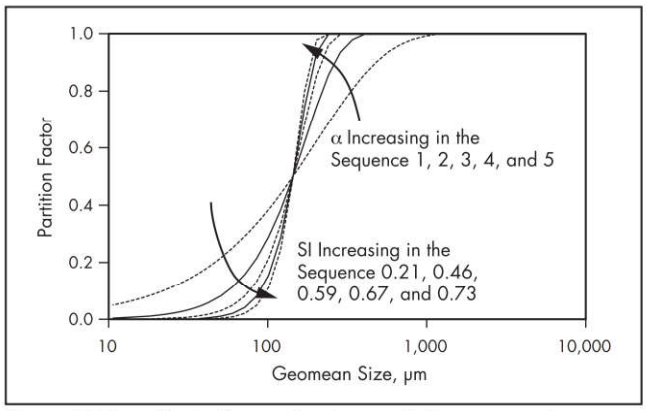

Figure 9 The effect of α on the shape of the corrected partition curve (Equation 11)

changing one will almost certainly require a compensating change in another to maintain a reasonable fit. Consequently, irregularities in one or two data points can have a deleterious effect on all parameter estimates. For example, and with reference to Table 7, if the size data in the very fine range drives an increase in *Rf*, one would observe increases in both α and *d*50*c* to compensate. The point to retain is that these parameters are not independent, and there is a series of combinations of these parameters that will give about the same results when the data are noisy.

To conclude this section, it is good to reflect on the findings of many researchers working on hydrocyclones. Corrected partition curves (c_i) can be normalized with size ($d_i/d50c$ on the x-axis) to form what is referred to as the reduced efficiency curve. (The c_i can be calculated from experimental data by rearranging Equation 10 and using the experimental partition factors, p_i.) For most normal operating regimes, and with geometrically similar hydrocyclones, the reduced efficiency (partition) curve retains the same shape (α is constant, although *d*50*c* and *Rf* can vary significantly). The reduced efficiency curves for the experimental data on both the soft and hard ores are shown in Figure 8.

The common empirical models of the hydrocyclone, as described in the main body of this chapter, have a series of correlations that allow one to estimate *d*50*c* and *Rf*, based on geometrical and operating inputs. These correlations then define the partition curve, which is at the heart of the classification process in this predictive mode.

MEASURES OF EFFICIENCY

In the preceding discussion, the parameter α was defined as the sharpness of separation for the more common corrected partition curve models of Equations 11 and 12. While α represents an important metric for separation efficiency and is explored in a little more detail in this section, it should be observed that *Rf* is also, in a way, a measure of efficiency. Following the thinking of the post-classification model in Figure 6, *Rf* can be seen as a measure of the fines that have been misplaced into the underflow stream. *Rf* is a complex function of many operating and design variables, but values in the range of 0.15 to 0.3 are preferred. Nevertheless, values as high as 0.4–0.5 are sometimes observed in practice. In terms of achieving an efficient separation process, the minimization of *Rf* is equally as important as maximizing α.

For hydrocyclones, Equation 11 α values in the range of 1.5 to 3 are quite common, and as Figure 9 shows, higher values mean sharper separations. As long as the same c_i model is being used, one can compare α's to compare separation efficiencies. Theoretically, perfect separation occurs for $\alpha = \infty$, but in practice, values of 5 or 6 (often seen for coarse vibrating screens) are near perfect.

A few other efficiency metrics were perhaps more common in the past, and they are reproduced for convenience. All are based on a few sizes that are easily extracted from the c_i model used in Equation 21. For these sizes for which $\hat{c} = 0.75$, hereafter termed *d*75*c*, and $\hat{c} = 0.25$, hereafter termed *d*25*c*.

Imperfection, I, is defined as

$$\mathrm{I} = \frac{[d75c - d25c]}{(2)(d50c)} \qquad \textbf{(EQ 24)}$$

Lower values of I imply sharper separations. Typical values for hydrocyclones would lie in the range of $0.25 \le \mathrm{I} \le 0.6$, corresponding to $3.1 \ge \alpha \ge 1.3$. For vibrating screens, these values would be $0.12 \le \mathrm{I} \le 0.2$, corresponding to $6.5 \ge \alpha \ge 3.9$.

The probable error of separation, or ecart probable moyen, Ep, is defined as

$$\mathrm{Ep} = \frac{[d75c - d25c]}{(2)} \qquad \textbf{(EQ 25)}$$

Lower values of Ep imply sharper separations. It is apparent that Ep = (I)(*d*50*c*), which implies that the two will show essentially identical trends as a function of α. In that regard, the dimensionless nature of I may make it a better metric for comparative purposes.

The sharpness index, SI, is defined as

$$\mathrm{SI} = \frac{d25c}{d75c} \qquad \textbf{(EQ 26)}$$

Higher values of SI imply a sharper separation, and perfect separation occurs at SI = 1. Typical values for hydrocyclones would lie in the range of $0.3 \le \mathrm{SI} \le 0.6$, corresponding to $1.3 \le \alpha \le 3.1$. For vibrating screens, these values would be $0.6 \le \mathrm{SI} \le 0.8$, corresponding to $3 \le \alpha \le 6.5$.

For illustrative purposes, the SI values were calculated for the various c_i curves and are also shown in Figure 9. To conclude this section, the three preceding metrics were computed for the hydrocyclones treating the soft and hard ores, as reported in Figure 10. These can be considered typical values.

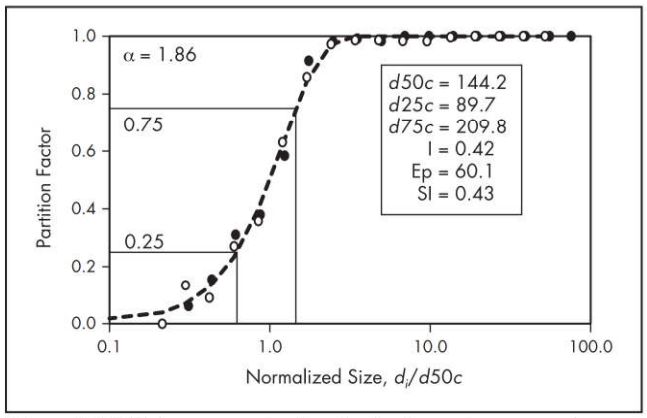

Figure 10 Efficiency metrics for the hydrocyclones treating soft and hard ores

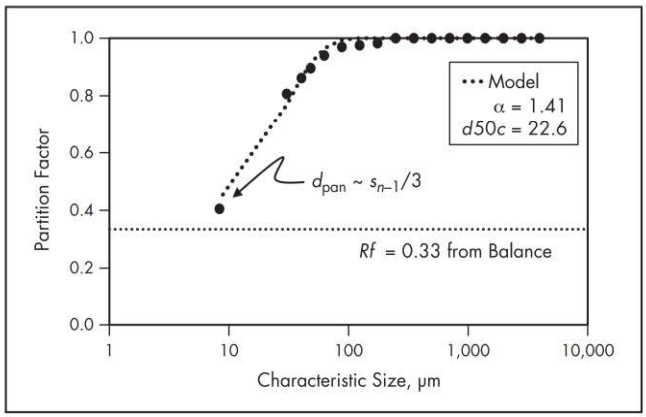

Figure 12 Partition curve for the fine-cut hydrocyclone using the d_{pan} approximation

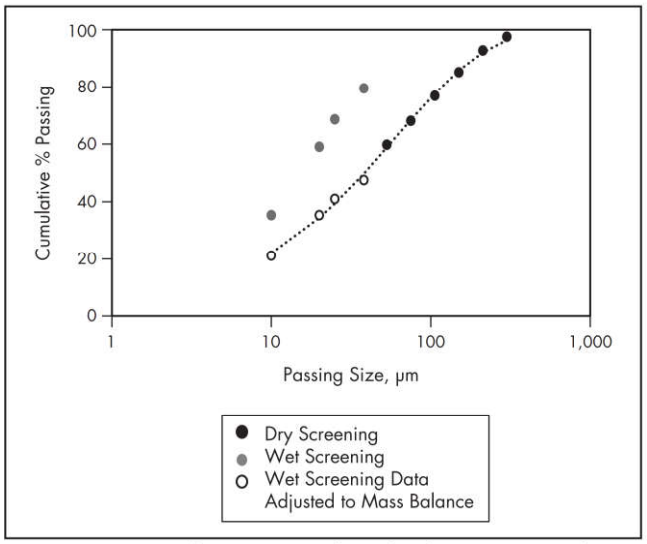

Figure 11 Dry and wet size analysis (with micro-sieving) to determine the full PSD curve

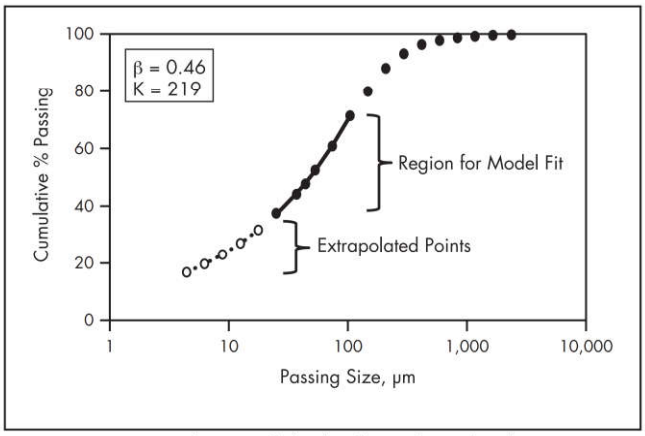

Figure 13 Extrapolation of the hydrocyclone feed size distribution using the Austin and Klimpel method

CHALLENGES WITH VERY FINE SEPARATIONS

In this section, two of the common challenges for very fine separations are addressed. The first is the measurement of particle size itself. Depending on the equipment available, one might be able to use a single device for measuring the particle size distribution, or PSD (e.g., a laser scattering system). However, in some cases one is forced to use sieves down to 400 mesh (37 μm) or 500 mesh (25 μm), combining both dry and wet sieving techniques, and then move to a completely different method such as sedimentation or cyclosizing, or even laser-based techniques. Changing methods means a change in the way the particle diameter is estimated, and that can require some manipulation to get a consistent estimate of the complete PSD. Herbst and Sepulveda (1985) have presented a methodology for making such an adjustment. For the purposes of this discussion, the author recommends that when sieves are employed for the coarser particle sizes, micro-sieving (same separation principles) be employed for the finer sizes whenever possible.

To illustrate, in Figure 11, dry screening was used down to 270 mesh (53 μm), followed by wet screening on the usual sieves for 400 mesh and 500 mesh, and finally wet micro-sieving for the very fine sizes (20 μm and 10 μm). In the figure, the dry and wet screening data are shown separately as solid circles, and the wet data are then adjusted for the sizing mass balance yielding the full PSD. To show the consistency, a Rosin–Rammler model (dotted line in Figure 11) was fit to the full size range, and it is clear that use of dry and wet sieving to very fine sizes essentially requires no additional manipulations.

The second challenge arises when the particle size analysis does not extend to the finer sizes, that is, where $d50c < s_{n-1}$ (the upper limiting size of the pan fraction). This can best be illustrated by example. The data in Table 8 are from a hydrocyclone making quite a fine cut and where the size analysis work was terminated at 25 μm. The geomean size d_1 is calculated by assuming the upper limiting size, $s_0 = \sqrt{2}\,s_1$.

Figure 12 shows the experimental and modeled partition curve results for the data of Table 8. The model parameters are presented in the figure. It is clear that, with the exception of the point at $d_{pan} = s_{n-1}/3$, the partition curve is only well defined at the coarser sizes. Clearly, the use of this approximation for d_{pan} helps, but the lack of definition of the curve in

Table 8 Mass balance for fine-cut hydrocyclone

Stream	Cyclone Feed (X)	Cyclone Overflow (O)	Cyclone Underflow (U)		
Relative Solids Mass Flow, %	100.00	25.76	74.24		
% Solids	52.41	29.89	70.96		
Passing Size, μm	Frequency, % retained	Frequency, % retained	Frequency, % retained	Geomean Size, μm	Partition Factor
3,327	0.06	—	0.08	3,956.5	1.00
2,362	0.20	—	0.26	2,803.3	1.00
1,651	0.19	—	0.26	1,974.8	1.00
1,168	0.37	—	0.50	1,388.7	1.00
833	0.50	—	0.67	986.4	1.00
589	0.94	—	1.27	700.5	1.00
417	1.42	—	1.91	495.6	1.00
295	3.16	—	4.26	350.7	1.00
208	5.09	—	6.86	247.7	1.00
147	8.09	0.54	10.71	174.9	0.98
104	8.61	0.82	11.31	123.6	0.98
74	10.55	1.24	13.78	87.7	0.97
53	8.31	1.94	10.52	62.6	0.94
44	4.78	1.94	5.77	48.3	0.90
37	3.59	1.93	4.17	40.3	0.86
25	6.59	4.94	7.16	30.4	0.81
Pan	37.56	86.66	20.51	8.3	0.41
Checks	100.00	100.00	100.00	—	—

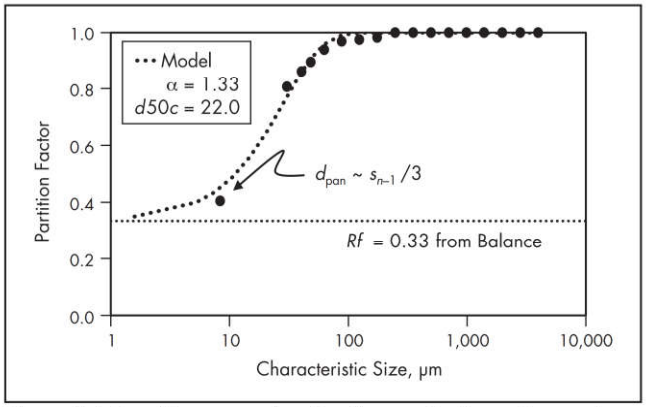

Figure 14 Partition curve for the fine-cut hydrocyclone using the Austin and Kimpel method

this region is a concern in terms of the quality of the parameter estimates.

Austin and Klimpel (1981) developed a clever scheme to analyze classifier data, and this includes the information carried by the pan fraction results. The authors use this method, although only for the pan fraction when $d50_c$ is less than s_{n-1}, as explained below.

Austin and Klimpel noted that the finer size regions of the hydrocyclone feed PSD can usually be well modeled using the Gates–Gaudin–Schuhmann equation, given by Equation 27. By extending the sizes into the very fine regions (say, down to 5 μm or smaller), one can estimate the cumulative fraction passing these finer sizes and, hence, the frequency retained on size data. In this case, a $\sqrt{2}$ series was selected to extend the hydrocyclone feed size distribution from the original s_{n-1} of 25 μm to include the following sizes: 17.7, 12.5, 8.8, 6.3, and 4.4, all in micrometers.

$$y = \left[\frac{s}{K}\right]^{\beta} \quad \textbf{(EQ 27)}$$

where

y = cumulative fraction passing
s = passing size
K = size modulus
β = distribution modulus

Figure 13 illustrates this process, showing the region over which the model parameters for Equation 27 are estimated and the subsequent results of the extrapolation.

If it is assumed that m new sizes have been added (here, $m = 5$), then the solution for the pan fraction partition factor is given in Equation 28:

$$\hat{p}_{pan} = \sum_{j=n}^{n+m} (\hat{p}_j f_j) \Big/ \sum_{j=n}^{n+m} (f_j) \quad \textbf{(EQ 28)}$$

Table 9 summarizes the calculations for the balanced data in Table 8, and Figure 14 shows the experimental and modeled partition data. Comparing the parameter values in Figures 12 and 14, it would seem that the approximation of $d_{pan} \sim s_{n-1}/3$ gives reasonable results. (Note that the new pan characteristic size in Table 9 is also estimated as $s_{n+m-1}/3$.)

Based on the Austin and Klimpel method mentioned previously, one can explain the approximation for the

Table 9 Results of applying the Austin and Klimpel technique

Passing Size, μm	Geomean Size, μm	Cumulative % Passing	Frequency, % retained	Extended Model Partition	Experimental Partition	Model Partition
3,327	3,956	99.94	0.06	1.00	1.00	1.00
2,362	2,803	99.75	0.20	1.00	1.00	1.00
1,651	1,975	99.55	0.19	1.00	1.00	1.00
1,168	1,389	99.18	0.37	1.00	1.00	1.00
833	986	98.68	0.50	1.00	1.00	1.00
589	700	97.74	0.94	1.00	1.00	1.00
417	496	96.32	1.42	1.00	1.00	1.00
295	351	93.16	3.16	1.00	1.00	1.00
208	248	88.07	5.09	1.00	1.00	1.00
147	175	79.98	8.09	1.00	0.98	1.00
104	124	71.37	8.61	1.00	0.98	1.00
74	88	60.83	10.55	0.99	0.97	0.99
53	63	52.52	8.31	0.96	0.94	0.96
44	48	47.74	4.78	0.91	0.90	0.91
37	40	44.15	3.59	0.86	0.86	0.86
25	30	37.56	6.59	0.77	0.81	0.77
17.7	21.0	31.69	5.86	0.65	**0.41**	**0.45**
12.5	14.9	27.05	4.64	0.56	Model Fit	
8.8	10.5	23.09	3.96	0.49	*Rf*	0.33
6.3	7.4	19.71	3.38	0.44	*m*	1.33
4.4	5.3	16.82	2.89	0.40	*d50c*	22.0
New pan	1.5		16.82	0.35	RSS	4.95E-03

Table 10 Air classifier partition data

Geomean Size, μm	Experimental Partition Factors	Finch Model Results	Austin et al. Model Results
210.49	1.00	1.00	1.00
148.74	1.00	1.00	1.00
104.88	1.00	1.00	1.00
74.46	1.00	1.00	1.00
52.65	0.96	0.97	0.97
37.23	0.77	0.77	0.77
26.32	0.50	0.50	0.52
18.58	0.41	0.39	0.38
13.14	0.30	0.35	0.33
9.23	0.36	0.36	0.35
6.53	0.41	0.37	0.40
4.69	0.43	0.43	0.44
1.33	0.46	0.46	0.46

Data adapted from Austin et al. 1984

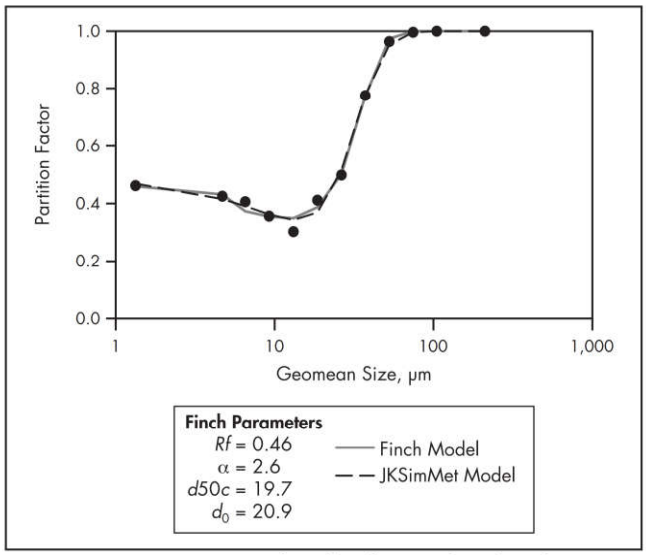

Figure 15 Partition curve data for the air classifier showing the Finch model parameters

characteristic size of the pan fraction, that is, $d_{pan} \sim s_{n-1}/3$, introduced earlier. The frequency form of the Gates–Gaudin–Schuhmann function in Equation 27 is given by Equation 29:

$$\frac{dy}{ds} = y' = \left[\frac{1}{K}\right]^{\beta}\left[\beta s^{\beta-1}\right] \quad \textbf{(EQ 29)}$$

The mass mean size for the pan fraction can then be estimated as

$$d_{pan} \approx \left[\int_0^{s_{n-1}} sy'ds \Big/ \int_0^{s_{n-1}} y'ds\right] = \left[\frac{\beta}{1+\beta}\right]s_{n-1} \quad \textbf{(EQ 30)}$$

Since the β values in the fine size regions of the hydrocyclone feed PSD often lie in the range of 0.45 to 0.55, assuming an average value of 0.5 yields the approximation $d_{pan} \sim s_{n-1}/3$.

As a rule of thumb, as long as the experimental partition factor for the size class n (p_n) is, say, less than 0.45 or so, using the simple approximation for d_{pan} is acceptable. For values of p_n greater than this level, one should strongly consider applying the Austin and Kimpel method, either as outlined here or the full method described in the reference article.

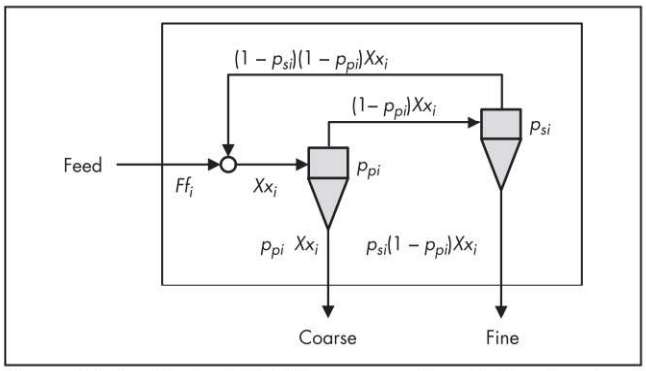

Figure 16 Austin et al. (1984) conceptual model for the air classifier

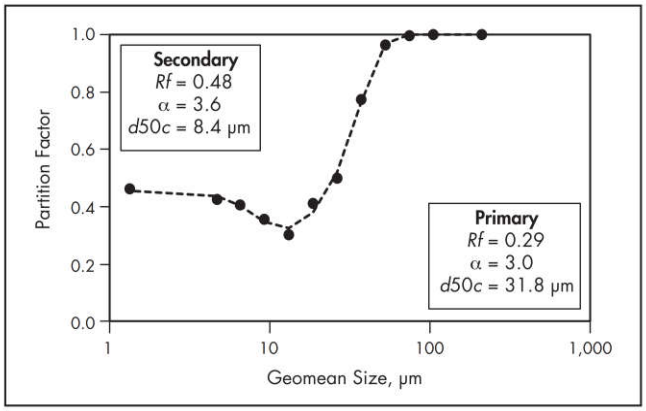

Figure 17 Partition curve data for the air classifier showing the Austin et al. (1984) model parameters

UNUSUAL PARTITION CURVES

The preceding discussion focused more on the usual sigmoidal partition curve; however, in some instances the shape of the experimental partition curve is not strictly sigmoidal. Finch (1983) was one of the first to publish on partition curve inflections in the fines sizes, and over the years many other authors have presented and explained similar findings. One of the best review/research papers was recently published by Eisele et al. (2013), and anyone interested in this topic is strongly encouraged to read this work.

For the purposes of this chapter, where the focus is on the partition curve for a hydrocyclone, there are two phenomena that can alter the shape of the more usual partition curve: (1) fines entrainment in the underflow stream (beyond the effect of *Rf*) and (2) multicomponent (heterogeneous) ores. Of the two, from an operational perspective, the second item is probably more important.

Fines Entrainment

The "fishhook" phenomenon usually occurs in the finer size ranges, say less than 50 μm and, more often, less than 20 μm. (The term *fishhook* derives from an unexpected upturn in the partition curve in the fine size region.) Explanations for this occurrence can involve flocculation or agglomeration, boundary layer entrainment, wake entrainment, dense medium effects, density effects, settling regimens, or the propagation of experimental errors (see Eisele et al. 2013 for more detail). The phenomenon is illustrated here by borrowing a data set (Austin et al. 1984) from a sampling experiment around an air classifier, as shown in the first two columns of Table 10.

Finch's approach to describe the partition curve was to reformulate Equation 21 as shown in Equation 31, borrowing from the phenomena of entrainment observed in flotation froths:

$$\hat{p}_i = Rf\left[\frac{d_0 - d_i}{d_0}\right] + \left[1 - 0.5^{\left(d_i / d_{50c}\right)^{\alpha}}\right] \quad \textbf{(EQ 31)}$$

where d_0 equals the size at which fines entrainment begins.

In this case, the first term is calculated only for the cases where $d_i < d_0$; otherwise, it is taken to be 0. Figure 15 shows the raw data and the Finch model fit, and the fishhook is quite apparent.

Users of JKSimMet will be familiar with the Whiten approach (described in Nageswararao et al. 2004) to account for a fishhook shape in the partition curve data. This four-parameter model is a little more involved, so it is not included here, although the results are shown in Figure 15 for comparative purposes. Nageswararao et al. (2004) have observed that in many cases—including the fishhook parameter in the JKSimMet model—the overall fit was improved, but statistical tests were not applied to assess whether this was simply the effect of additional parameters or whether the partition curve required it.

In their work on air classifiers, Austin et al. (1984) developed a conceptual model based on mechanisms at work in this device, and this is shown in Figure 16. The model that arises from this formulation is given by Equation 32, and the fit is presented in Figure 17.

$$\hat{p}_i = \frac{\hat{p}_{pi}}{\left[1 - (1 - \hat{p}_{si})(1 - \hat{p}_{pi})\right]} \quad \textbf{(EQ 32)}$$

where

$\hat{p}_{pi}$ = primary separation partition curve, same form as Equation 21

$\hat{p}_{si}$ = secondary separation partition curve, same form as Equation 21

Clearly, more complex partition curve shapes call for more complex models. In this case, Finch uses four parameters and Austin et al. (1984) use six parameters. Based on Partial F testing, there is no statistical justification to go with the more complex model of Austin et al.although conceptually it has some merit. For parameters to be useful metrics in assessing performance, parsimony is key (i.e., two or three, and possibly four, parameters are "manageable"). Beyond that, one might just as well use generic functional forms (e.g., high-order polynomials or splines) to connect the points.

Multicomponent Ores

For purposes of this discussion, the author considers multicomponent ores to include significant quantities of minerals with quite different specific gravities. Since hydrocyclone classification involves settling velocities, particle mass is important, and that depends on both size and specific gravity (sg). A particularly good example of this in the mining industry is iron ore processing, where in many cases the ores can be considered to consist of silica (sg = 2.65) and magnetite or hematite (sg = 4.9–5.2).

Eisele et al. (2013) have shown how plateaus or humps are formed in partition curves when synthetic mixtures of

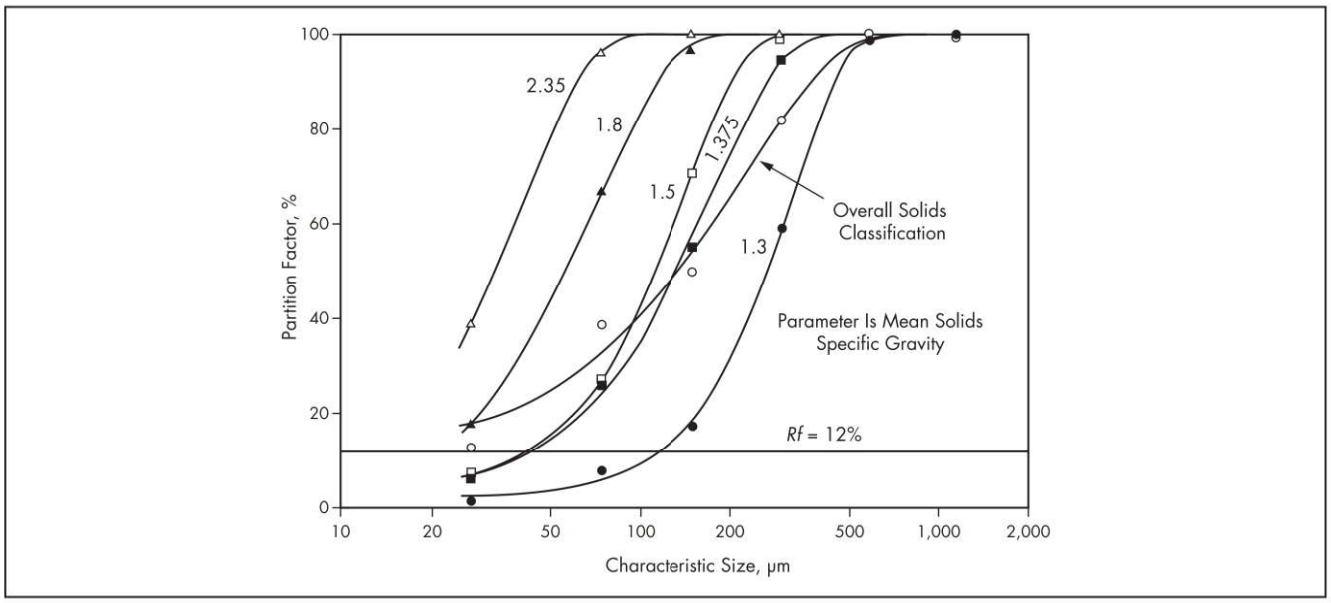

Source: Flintoff et al. 1987

Figure 18 Partition curves for coal slurry in a hydrocyclone

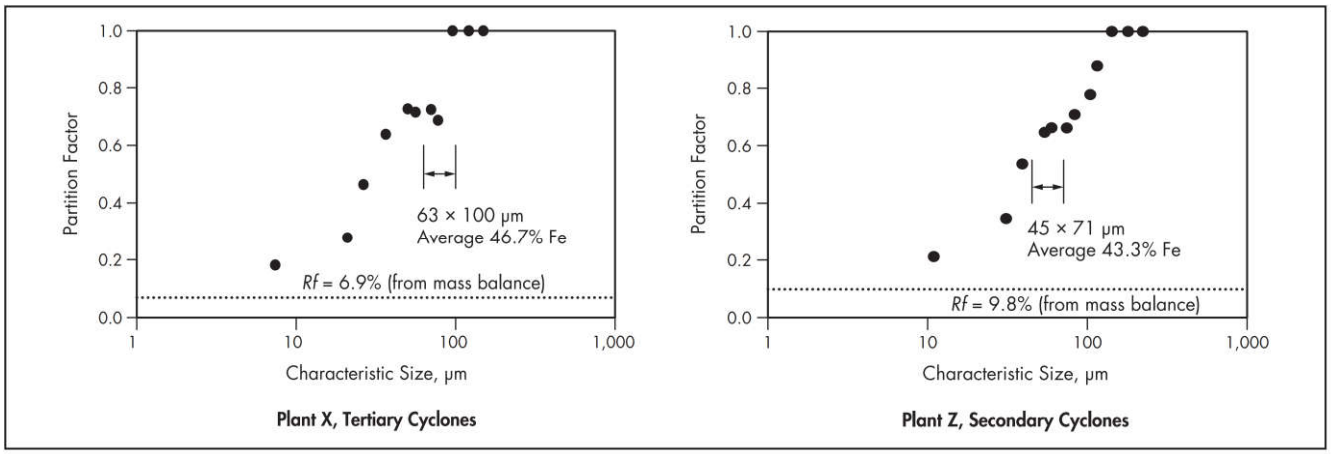

Figure 19 Partition curves for two magnetite plants from experimental data

silica and magnetite are mixed and fed to a hydrocyclone. They have also shown similar partition curve shapes from plant sampling campaigns in a magnetite concentrator.

Not all multicomponent ores give rise to unusual partition curve shapes. A good example of this from the mining industry is a hydrocyclone treating coal. In this case, there is essentially a continuous range of specific gravity components in the solids, and the net effect is that a reasonable overall partition curve shape, albeit with a low α value, is derived. However, if one submits the cyclone products to sink/float analyses to separate the specific gravity classes by size, a clearer picture emerges. Figure 18 illustrates this situation.

It is clear in Figure 18 that the cut size ($d50c$) is dependent on the specific gravity and the functional form follows from the settling theory as shown in Equation 33. Minerals with higher specific gravities have finer cut sizes:

$$d50c \propto \frac{1}{[\rho_s - 1]^k} \quad \textbf{(EQ 33)}$$

where

ρ_s = specific gravity of the solid component
k = exponent 0.5 for Stokesian conditions and 1.0 for Newtonian conditions—experimental values vary from theory (e.g., for the data in Figure 16, $k \approx 1.13$ [Flintoff et al. 1987])

The behavior of the curves in the very fine sizes may seem a little odd, as they do not appear to asymptotically approach *Rf*, the lighter fractions showing lower values than the fractional bypass of water. Here, this is likely the result of dense medium separation effects in the neighborhood of the apex, something that is exploited in automedium hydrocyclones for fine coal preparation applications.

Coming back to the two-component iron ore system, Figure 19 shows the results for two different magnetite plants, where the hydrocyclones are producing final comminution circuit product, which, in turn, will get a final cleaning by magnetic separation. The humps or plateaus are very clear in

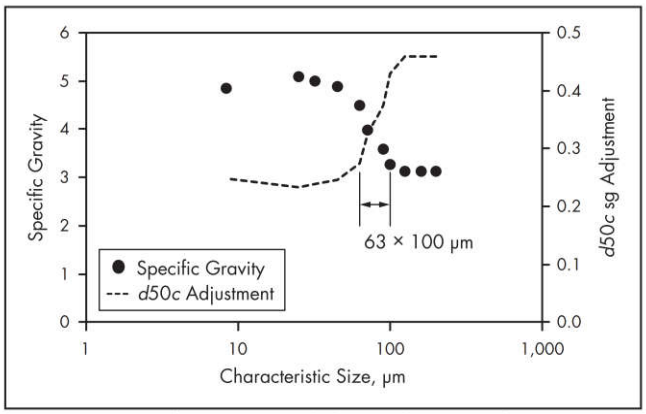

Figure 20 Specific gravity and *d*50*c* adjustment factors as a function of size for plant X

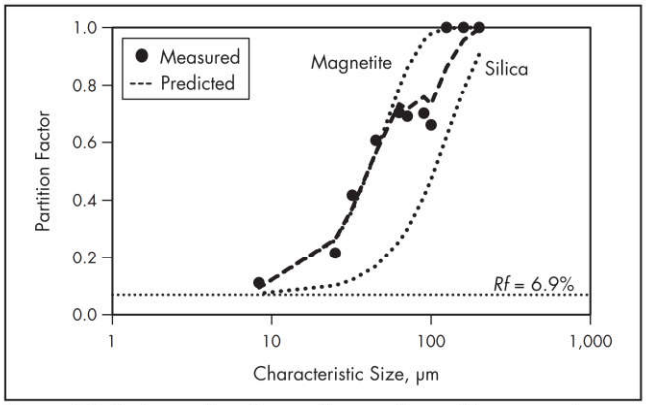

Figure 21 Estimated and actual overall partition curve for plant X

this case, and as Eisele et al. (2013) point out, these are exacerbated by the concentration of fine liberated magnetite in the hydrocyclone underflow stream, which inevitably returns to the hydrocyclone feed after passing through a ball mill.

In both cases, one can see that a significant portion of a middlings size class (~45% Fe) reports to the hydrocyclone overflow, and since magnetic separators are designed to recover all particles that exhibit magnetic properties, this material contaminates the final concentrate and can contribute to a lower grade. This is one of the reasons that fine screens are seeing more use in these circuits (e.g., scavenging the coarse lower-grade material from the hydrocyclone overflow and directing it back to the ball mill to get to premium product grade levels of 67%–68% Fe or higher).

Understanding the reasons for the plateau region in Figure 19 is a little more challenging than making inferences from synthetic mixtures. This is more like the coal problem, although because of prior magnetic separation steps, much of the free silica has been removed, so it is not a natural feed in that sense.

For plant X, there were some liberation data on the ore at the time the sampling campaign was completed, and in all cases, the size fractions were assayed for %Fe. These liberation data, combined with the preceding information, allowed for decomposition of the hydrocyclone feed into three components: free magnetite, locked magnetite, and free silica. In the case of the locked particles, the specific gravity varies with the iron content, which varies as a function of size. Figure 20 shows the estimated variation of particle specific gravity with size. In this case, k in Equation 33 was estimated as 1.03, and the $d50c$ adjustment from the equation is also shown on the figure. In the range of the plateau, one can clearly see that while size is increasing (which should increase the partition factor), the density is dropping, which has the effect of translating the actual partition curve to the right and driving the partition factor down. The net result is that during this transient in the average particle density, the overall partition curve will show some sort of inflection, and those displayed in Figure 19 are typical.

Using a model of the form given by Equation 21, with the specific gravity correction of Equation 33, the overall predicted partition curve was computed based on individual component behavior. These results are shown in Figure 21, and given the initial assumptions, they seem quite reasonable. Note that the free magnetite and free silica curves are included for reference.

It may be possible to use simpler modeling approaches to characterize the curve, but for meaningful parameter estimation and understanding of where the inflection forms and its extent, much more information is required. Incorporating this kind of structure into process simulation packages like JKSimMet is in progress (e.g., Narasimha et al. 2012).

CONCLUSIONS

The partition curve is ubiquitous in characterizing classification processes based on the physical attributes of the particles. They serve as a diagnostic tool for assessing the performance of these units through parameter estimation and possible comparison with other parameter data. In the case of some unit operations, like the hydrocyclone and screens, they lie at the heart of more comprehensive empirical models, which are embedded in simulation software, and are useful in process analysis, design, and optimization.

Despite their apparent mathematical simplicity, the work required to get a good estimate of a partition curve is time-consuming, and every effort must be made to comply with the best practices for process surveys. The raw data can be used in that state, but it is better to massage it with mass balance software before getting into the modeling work. In porphyry copper (not massive sulfides) and gold ores, it is common to be able to use two- or three-parameter models. Statistical comparison can be used to select the best model and, in itself, can be another useful diagnostic around data quality. In the case of multicomponent ores (e.g., iron ore, coal, or massive sulfide deposits), specific gravity variation can complicate the partition curve analysis, although work on multicomponent simulation packages should make this easier in the future. The fishhook phenomenon that is visible in some partition curves can usually be handled by adding a single parameter, although a mechanistic interpretation of this can sometimes be difficult.

REFERENCES

Austin, L., and Klimpel, R. 1981. An improved method of analyzing classifier data. *Powder Technol.* 29:277–285.

Austin, L., Klimpel, R., and Luckie, P. 1984. *Process Engineering of Size Reduction: Ball Milling.* Littleton, CO: SME-AIME. pp. 328–329.

De Lange, T., and Venter, P. 1987. The use of simulation Tromp partition curves in developing the flowsheet of plant extensions at Grootegeluk coal mine. In *Proceedings of the 20th International Symposium on the Application of Computers and Mathematics in the Mineral Industries*, Vol. 2. Johannesburg: Southern African Institute of Mining and Metallurgy. pp. 295–311.

de Levie, R. 1999. Estimating parameter precision in nonlinear least squares with Excel's Solver. *J. Chem. Educ.* 76:1594–1598.

Eisele, T., Jeltema, C., Walqui, H., and Kawatra, S. 2013. Coarse and fine fish hook inflections in hydrocyclone efficiency curves. *Miner. Metall. Process.* 30(3):137–144.

Finch, J. 1983. Modelling a fish-hook in hydrocyclone curves. *Powder Technol.* 36:127–129.

Flintoff, B., Plitt, L., and Turak, A. 1987. Cyclone modelling: A review of present technology. *CIM Bull.* 80(905):39–49.

Herbst, J., and Sepulveda, J. 1985. Characterization of test samples—Particle size analysis. *SME Mineral Processing Handbook.* Edited by N.L. Weiss. Littleton, CO: SME-AIME. pp. 30:20–30:43.

Hodouin, D., Kasongo, T., Kouame, E., and Everell, M. 1981. BILMAT: An algorithm for materials balancing mineral processing circuits. *CIM Bull.* 64(833):123–131.

Hodouin, D., Bazin, C., and Trusiak, A. 1984. Reliability of calculation of mineral process efficiencies and rate parameters from balanced data. In *Control '84: International Symposium on Automatic Control in Mineral Processing and Process Metallurgy.* Edited by J. Herbst, K. Sastry, and D. George. Littleton, CO: SME-AIME. pp. 133–144.

Laguitton, D., ed. 1985. *The SPOC Manual*. Ottawa, ON: Energy, Mines and Resources Canada, Canada Centre for Mineral and Energy Technology.

Lynch, A., and Rao, T. 1975. Modelling and scale-up of hydrocyclone classifiers. In *Proceedings of the 11th International Mineral Processing Congress.* Cagliari, Sardinia: Istituto di Arte Mineraria e Preparazione dei Minerali. pp. 245–269.

Mular, A. 1979. Data adjustment procedures for mass balances. In *Computer Methods for the 80s in Mineral Processing*. Edited by A. Weiss. Littleton, CO: SME-AIME. pp. 843–849.

Nageswararao, K., Wiseman, D., and Napier-Munn, T. 2004. Two empirical hydrocyclone models revisited. *Miner. Eng.* 17:671–687.

Narasimha, M., Mainza, A., and Holtham, P. 2012. Multicomponent modeling concept for a hydrocyclone classifier. In *Proceedings of the XXVI International Mineral Processing Congress*. New Delhi: Indian Institute of Metals. pp. 3696–3707.

Plitt, L. 1971. The analysis of solids-solid separations in classifiers. *CIM Bull.* 64:42–47.

Wei, J., and Realff, M. 2005. Design and optimization of drum-type electrostatic separators for plastics recycling. *Ind. Eng. Chem. Res.* 44(10):3503–3509.

Wiegel, R. 1979. The practical benefits of improved metallurgical balance techniques. SME Preprint No. 79-92, Littleton, CO: SME.

Wills, B., and Finch, J. 2016. Chapter 9, Classification. In *Wills' Mineral Processing Technology: An Introduction to the Practical Aspects of Ore Treatment and Mineral Recovery.* Oxford; Waltham, MA: Butterworth-Heinemann.

PART 5

Transport and Storage